

Molecular-Scale Speciation of Zn and Ni in Soil Ferromanganese Nodules from Loess Soils of the Mississippi Basin

ALAIN MANCEAU,^{*,†,‡}
NOBUMICHI TAMURA,[†]
RICHARD S. CELESTRE,[†]
ALASTAIR A. MACDOWELL,[†]
NICOLAS GEOFFROY,[‡]
GARRISON SPOSITO,[§] AND
HOWARD A. PADMORE[†]

Advanced Light Source, Lawrence Berkeley National Laboratory, One Cyclotron Road, Berkeley, California 94720, Environmental Geochemistry Group, LGIT–Maison des Geosciences, University J. Fourier and CNRS, 38041 Grenoble Cedex 9, France, Geochemistry Department, Earth Sciences Division, Lawrence Berkeley National Laboratory, University of California, Berkeley, California 94720

Determining how environmentally important trace metals are sequestered in soils at the molecular scale is critical to developing a solid scientific basis for maintaining soil quality and formulating effective remediation strategies. The speciation of Zn and Ni in ferromanganese nodules from loess soils of the Mississippi Basin was determined by a synergistic use of three noninvasive synchrotron-based techniques: X-ray microfluorescence (μ XRF), X-ray microdiffraction (μ XRD), and extended X-ray absorption fine structure spectroscopy (EXAFS). We show that Ni is distributed between goethite (α -FeOOH) and the manganese oxide lithiophorite, whereas Zn is bound to goethite, lithiophorite, phyllosilicates, and the manganese oxide birnessite. The selective association of Ni with only iron and manganese oxides is an explanation for its higher partitioning in nodules over the soil clay matrix reported from soils worldwide. This could also explain the observed enrichment of Ni in oceanic manganese nodules. The combination of these three techniques provides a new method for determining trace metal speciation in both natural and contaminated environmental materials.

Introduction

Since their discovery in Essex, U.K., in the beginning of the last century, ferromanganese micronodules have been found to be widespread at the earth's surface, often amounting to several percent by mass in soils; their micromorphological, mineralogical, and chemical characteristics have been investigated frequently (1–3). These concretions, usually subrounded in shape, with diameters ranging from a few

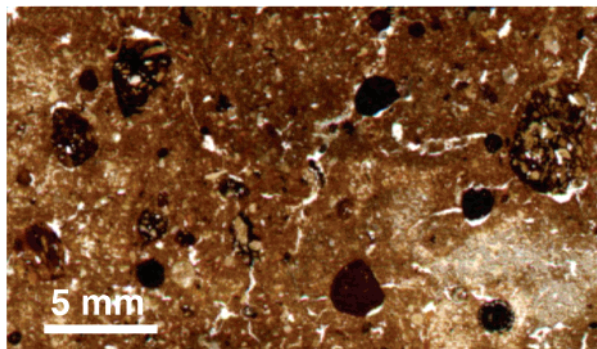


FIGURE 1. Photomicrograph of a soil thin section (30 μ m thick) containing embedded ferromanganese concretions. Mineralogical analyses indicate that quartz, phyllosilicate, feldspar, titanium oxides, and carbonates are the principal crystalline components of the nodules and the soil matrix. This mineralogical similarity between the concretions and the soil matrix points to an in situ formation of nodules. Soil micronodules are always enriched in Fe, Mn, and trace metals relative to the soil matrix. Segregation of Fe and Mn is responsible for cementation of the soil grains and results from the alternation of oxidation and reduction conditions (i.e., seasonal waterlogging).

millimeters to less than 1 mm are brown to dark-brown in color depending on the Fe/Mn ratio (Figure 1). Inspection of thin sections with an optical microscope shows that the nodules contain grains of primary minerals (quartz, feldspars, micas) cemented with an ochreous-brown or dark nonpolarizing matrix consisting chiefly of iron, manganese oxides, and phyllosilicates. The mineralogical similarity between the concretions and the adjacent soil matrix indicates that they are formed in place and not transported, despite having distinct borders (4). Nodule formation in most soils results from their changing moisture regime (5, 6). During wet periods, Fe(III) and Mn(III/IV) are reduced and dissolve in pore waters, while during dry periods they reprecipitate and cement soil particles (7). Repetition of this process eventually forms millimeter-sized nodules that often exhibit the concentric layering suggestive of seasonal growth. Interestingly, this localized increase in the concentrations of Fe and Mn in soil is always accompanied by a high partitioning of trace metals. For example, in Sicilian nodules, high enrichment factors (ratio of metal concentration in the nodules to that in the soil matrix) were observed for Mn (296), Co (93), Ce (45), Pb (31), Ba (18), Ni (17), Cd (15), and Fe (2.6) (8). Zinc was weakly partitioned into the nodules (1.5), despite its known high affinity for manganese and iron oxides (8). Similar results were obtained for New Zealand nodules (9). In contrast, ferromanganese coatings on river sediments in England were found to contain high concentrations of Zn along with Pb, Cu, and Cd (10).

Although the enrichment of trace metals in soil micronodules is regarded as an efficient and robust process for their sequestration, the crystal chemistry of the sequestered elements remains unknown. The principal reasons for this include low concentrations relative to the detection limit of conventional laterally resolved analytical and crystallographic probes, the partitioning into coexisting minerals, the nanoscale size of most reactive soil particles, the difficulty of identifying the mineral species into which trace metals are bound, and the multiplicity of sorption mechanisms. These long-standing impediments to understanding at the molecular level how trace metals interact and are sequestered by soil constituents are now surmountable using X-ray

* Corresponding author phone: 33 (0)4 76 82 80 15; fax: 33 (0)4 76 82 81 01; e-mail: Alain.Manceau@ujf-grenoble.fr.

[†] Advanced Light Source, Lawrence Berkeley National Laboratory.

[‡] University J. Fourier and CNRS, Grenoble, France.

[§] Geochemistry Department, Earth Sciences Division, Lawrence Berkeley National Laboratory, University of California.

techniques developed at third generation synchrotron facilities (11). We show here that these problems can in fact be overcome by combining X-ray microfluorescence (μ XRF), X-ray microdiffraction (μ XRD), and extended X-ray absorption fine structure (EXAFS) spectroscopy applied in situ without disrupting the natural soil matrix. μ XRF is used to map the distribution of trace contaminants among coexisting mineral phases in a natural matrix; μ XRD allows identification of nanoscale particles, the most reactive toward the trace metals; and EXAFS spectroscopy provides the mechanism of metal sequestration by the host minerals at the molecular scale.

Materials and Methods

The micronodules studied here were collected in the silty uplands of the Mississippi Basin and were previously characterized by Rhoton et al. (12). Their Fe concentration was typically twice that of Mn, as estimated from the $K\alpha(\text{Fe})/K\alpha(\text{Mn})$ fluorescence intensity ratio, and about 2 or 2.5 orders of magnitude higher than the Zn and Ni concentrations, respectively. Their chemical heterogeneity was determined more precisely by analyzing 20 individual nodules using inductively coupled plasma atomic emission spectroscopy (ICP-AES) and inductively coupled plasma mass spectroscopy (ICP-MS). These analyses gave $[\text{Fe}] = 57526$ ($\sigma = 21213$), $[\text{Mn}] = 25592$ ($\sigma = 17716$), $[\text{Zn}] = 76$ ($\sigma = 51$), and $[\text{Ni}] = 67$ ($\sigma = 21$) mg/kg. The σ variability is comparable to that measured for Sicilian nodules (8).

X-ray fluorescence spectra and diffraction patterns were recorded on Beamline 7.3.3 at the Advanced Light Source (ALS, Berkeley, CA), and EXAFS spectra were recorded on Beamline BM32 at the European Synchrotron Radiation Facility (ESRF, Grenoble, France). The μ XRF maps were obtained by scanning the soil nodules under a monochromatic beam with an energy of 10 keV and a beam size on the sample of $10 \mu\text{m H} \times 25 \mu\text{m V}$, while recording the X-ray fluorescence with a Ge solid-state detector. μ XRD patterns were collected at selected points of interest with the same lateral resolution as μ XRF using a 1024×1024 pixels CCD camera and an exposure time of 10–20 min. μ XRF and μ XRD data were collected in reflection geometry mode by inclining the sample at $6^\circ \theta$ (13). Fluorescence-yield zinc K-edge EXAFS spectra were collected on a powdered pellet of 10 nodules using a 30-Ge solid-state detector. EXAFS measurements were carried out by orienting the sample vertically to 45° to both the X-ray beam and the solid-state detector. A large set of Zn K EXAFS reference spectra from previous studies (14–22) were used for EXAFS fitting. This extensive database includes primary Zn minerals (sphalerite, chalcophanite, zincite, gahnite, hemimorphite, willemite), hydroxylated Zn minerals and precipitates (phosphophyllite, hopeite, parahopeite, phosphate dihydrate, and Zn-substituted lithiophorite, goethite, hematite, kerolites, and zinc–aluminum hydrotalcite), carbonates (smithsonite, hydrozincite), sorption substrates at different surface loadings (Zn-sorbed birnessites, ferrihydrites, kerolites, and hectorites; both inner- and outer-sphere surface complexes), and Zn complexation to organics (phytate, low weight organic acids, humic and fulvic acids, bacterial exopolymers, and fungi cell walls).

Results and Discussion

Metal Partitioning and Mineral Species. Eight nodules were examined, and the mineralogy and crystal chemistry of Zn and Ni are completely represented by the three samples in Figure 2. In contrast to the bulk analyses, μ XRF maps show that individual nodules are highly heterogeneous at the micrometer scale, containing distinct areas of concentrated Fe, Mn, Ni, and Zn. Nodule 1 shows, on average, little

correlation between Fe and Mn ($r_{\text{Fe-Mn}} = 0.62$), but visual inspection of the maps shows that the degree of correlation varies laterally. The richest Fe areas in the outer region are strongly depleted in Mn, whereas the inner region contains areas of both high Mn and high Fe. Zn and Ni are strongly correlated with Fe ($r_{\text{Fe-Zn}} = 0.84$, $r_{\text{Fe-Ni}} = 0.88$) and to a lesser extent with Mn ($r_{\text{Mn-Zn}} = 0.71$, $r_{\text{Mn-Ni}} = 0.78$). The relatively high $r_{\text{Mn-Ni}}$ value does not necessarily indicate that a Ni fraction is actually associated with Mn but instead can result from the incomplete separation of Fe and Mn in the core of the nodule. μ XRD analysis revealed that the outermost Fe-rich region consists of finely dispersed goethite ($\alpha\text{-FeOOH}$). Quartz, feldspar, titanium oxide, and carbonate grains also were detected. The Fe–Mn core contains essentially ferrihydrite ($\delta\text{-FeOOH}$) and vernadite (randomly layered birnessite, $\delta\text{-MnO}_2$) in variable proportions depending on the Fe/Mn ratio and a minor amount of goethite (23, 24). Therefore, the highest Zn and Ni concentrations are with goethite in this nodule.

Mn, Fe, Zn, and Ni were also unevenly distributed in nodule 2 (Figure 2b), which showed a moderate overall correlation between Fe and Mn ($r_{\text{Fe-Mn}} = 0.78$). However, the central region is high in Fe and Mn, whereas the external Fe layer is depleted in Mn. As with the previous nodule, this result illustrates the spurious meaning of elemental correlations calculated solely from total chemical analyses. Nodule 2 possesses a Zn–Ni “hot spot”, about $80 \times 80 \mu\text{m}^2$ in area, that is strongly correlated with Mn. The core of the nodule is enriched in Zn as well but devoid of Ni, suggesting that nodule 2 contains two major Zn species but only a single Ni species, one which also contains Zn. The mineralogical nature of the minute Mn grain containing both Zn and Ni was identified by μ XRD as lithiophorite, a $\text{MnO}_2\text{-Al}(\text{OH})_3$ mixed-layer phyllosilicate (Figure 3). In the two-dimensional XRD pattern, Bragg reflections from this grain formed a continuous Debye ring, characteristic of a powder diffraction pattern. The lithiophorite is therefore very fine-grained like most natural reactive particles. Vernadite, together with phyllosilicate, was positively identified in the central region by μ XRD (Figure 2b). Vernadite and lithiophorite are considered to be the two predominant Mn mineral species in near-surface environments (25–29), but their defective structure (vernadite) and small particle size pose major problems for identifying them by conventional XRD. The combination of μ XRF and μ XRD provides the necessary lateral resolution for establishing their presence and role in the sequestration of trace metals.

Two Zn fractions were also detected in nodule 3 (Figure 2c). In the first, Zn is concentrated with Ni and Mn at the core, which, according to μ XRD, contains lithiophorite and phyllosilicate, a geochemical association already found in nodule 2. The second fraction of Zn has a uniform background signal distributed throughout the nodule and likely as well in the central region where it is masked by the Zn,Ni lithiophorite species. Clearly, this second Zn fraction is not bound either to iron or manganese oxides, because neither the Fe nor the Mn map shows areal contours similar to the Zn map (the Mn map exhibits pockets of manganese in the outer region forming an incomplete ring). μ XRD patterns collected in Zn-containing (but Fe- and Mn-depleted) regions showed the presence of major dioctahedral phyllosilicates and secondary iron/manganese oxides (Figure 2c). Therefore, the second Zn fraction likely corresponds to a Zn-containing phyllosilicate. Zn is known to have a high affinity for sheet silicates and, for example, is abundantly present in this mineral host in Zn-contaminated soils from France and Belgium (19).

Close examination of the phyllosilicate diffraction lines shows that they contain higher-intensity spots, arising from micrometer-sized grains, superimposed on the continuous

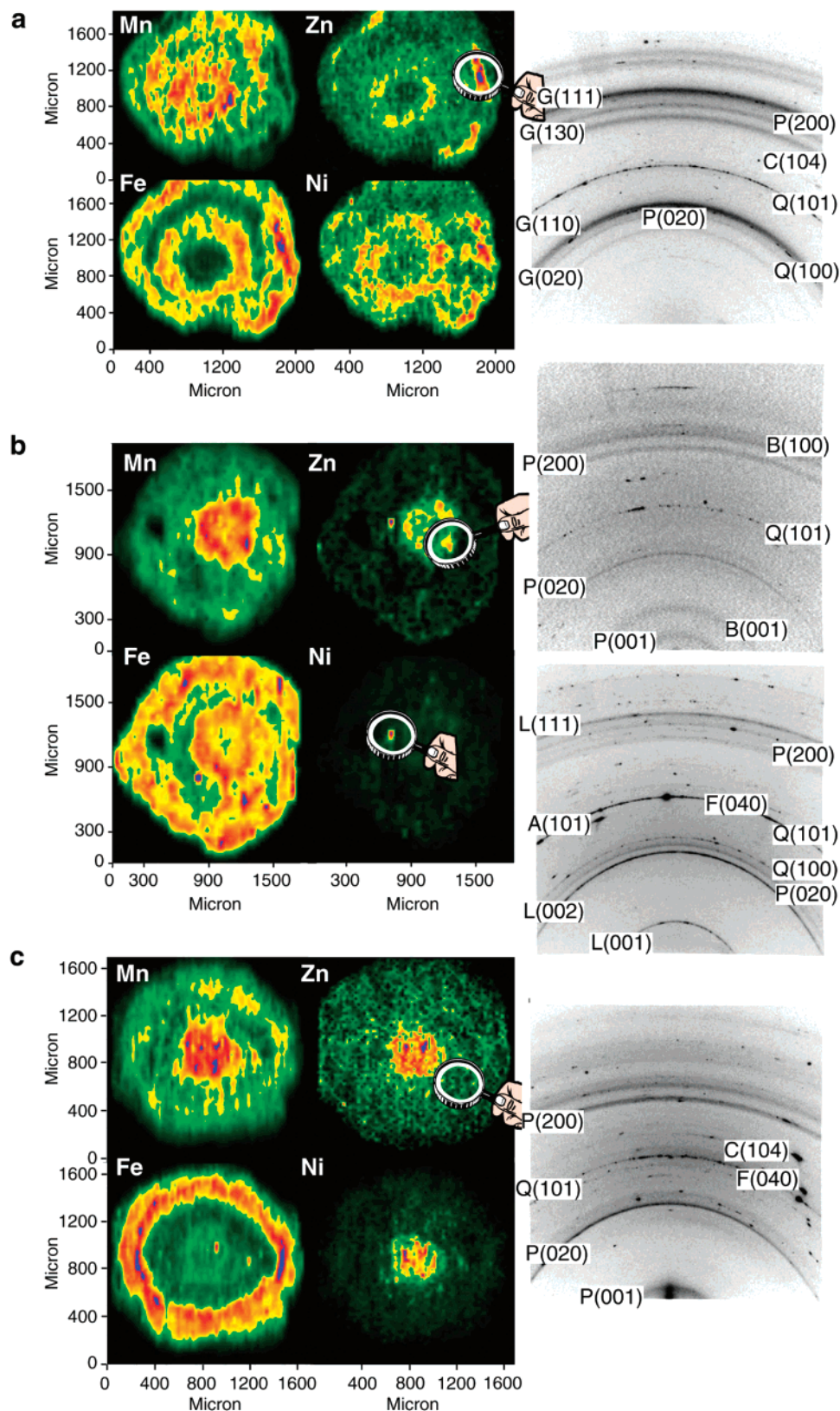


FIGURE 2. Synchrotron-based micro-X-ray fluorescence (μ XRF) maps showing the distribution of metals in three ferromanganese nodules. The maps were obtained by scanning the soil nodules under a monochromatic beam ($E = 10$ keV; beam size on the sample: $10 \mu\text{m H} \times 25 \mu\text{m V}$; step size: $32 \times 32 \mu\text{m}$ (a), $42 \times 42 \mu\text{m}$ (b), $25 \times 25 \mu\text{m}$ (c); counting time: 5–8 s/point). μ XRD patterns were collected at selected points of interest using an exposure time of 10–20 min and an incident X-ray energy of $E = 6.0$ (a, b) and 6.3 keV (c). B, hexagonal birnessite (main diffraction peaks at 7.1 – 7.2 , 2.45 , and 1.41 \AA); G, goethite (main diffraction peaks at 4.18 and 2.69 \AA); L, lithiophorite (main diffraction peaks at 9.4 , 4.7 , and 2.37 \AA); P, phyllosilicate (main diffraction peaks at 4.45 – 4.48 , 2.55 – 2.58 , and 1.50 \AA); Q, quartz; F, feldspar; A, anatase; C, calcite. hkl reflections are in parentheses. In panel a, Ni and Zn are associated with goethite (α -FeOOH); in panel b, Ni is associated with lithiophorite, and Zn is associated with lithiophorite and birnessite; in panel c, Ni is associated with lithiophorite, and Zn is associated with lithiophorite and phyllosilicate.

One-component simulation

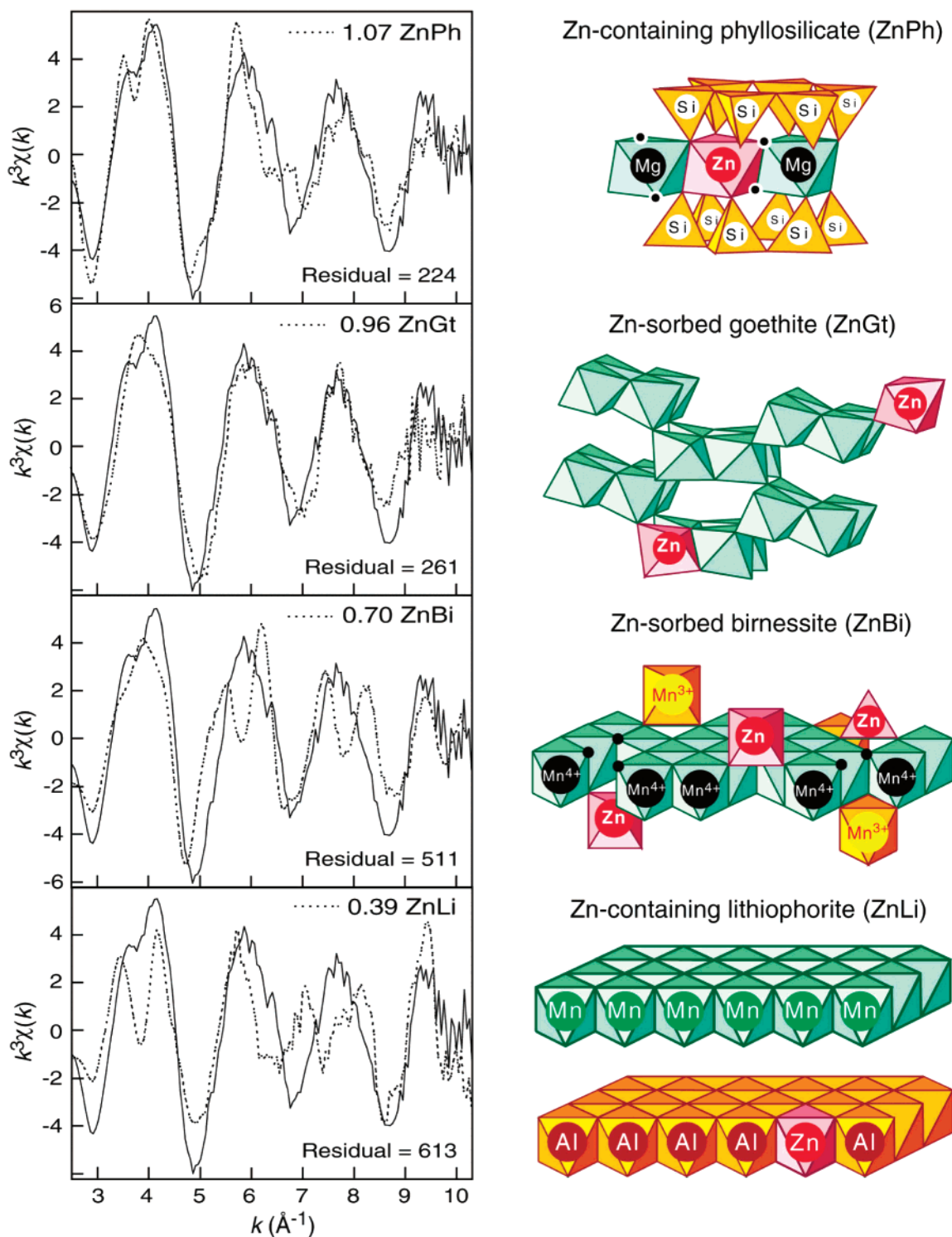


FIGURE 3. Zn K-edge EXAFS spectrum collected from the powder of 10 nodules (solid line) and one-component least-squares fitting from a library of Zn model compounds (dotted line). The phyllosilicate reference is a kerolite $[\text{Si}_4(\text{Zn}_{0.4}\text{Mg}_{2.6})\text{O}_{10}(\text{OH})_2]$ in which Zn is substituted for Mg in the octahedral sheet (19). In Zn-sorbed goethite, Zn octahedra form double corner-sharing and edge-sharing surface complexes. The hexagonal birnessite reference has a Zn/Mn ratio of 0.122 (33% of Zn is tetrahedrally coordinated and 67% is octahedrally coordinated) (21, 39). In lithiophorite, Zn substitutes for Li in the $\text{Al}(\text{OH})_3$ layer (29).

diffraction rings from finely dispersed particles. We observed this superposition effect many times; it is characteristic of an admixture of micaceous particles and minute smectitic clays. These two phyllosilicate families were always observed in the soil concretions and in the surrounding matrix. It was almost impossible to find regions containing only iron or

manganese oxides. For example, the four two-dimensional μXRD patterns presented in Figure 2 all contain diffraction rings at 4.45–4.48 and 2.55–2.58 \AA , typical of the 020–110 and 130–200 reflections that characterize sheet silicates. A peak at 1.50 \AA was observed systematically at higher diffraction angles, thus indicating the mostly dioctahedral

structure of these minerals. Elemental correlation coefficients for nodule 3 can be interpreted readily on the basis of these results. Little correlation was obtained for Fe and Mn ($r_{\text{Fe-Mn}} = 0.69$), in agreement with the nonoverlapping contour maps for these two elements. The Mn–Zn correlation is moderate ($r_{\text{Mn-Zn}} = 0.76$) because of the partial association of Zn with phyllosilicate, whereas the Mn–Ni correlation is higher ($r_{\text{Mn-Ni}} = 0.82$) since Ni is uniquely bound to lithiophorite. Correlations between Fe and Zn ($r_{\text{Fe-Zn}} = 0.44$) or Fe and Ni ($r_{\text{Fe-Ni}} = 0.33$) are low, as expected.

Speciation of Zn. The nature and proportion of Zn species in the soil nodules were determined by EXAFS spectroscopy. On the basis of our microanalyses, Zn is bound to four mineral species: goethite, phyllosilicate, hexagonal birnessite, and lithiophorite. Therefore, the bulk EXAFS spectrum can be deconvoluted as a weighted sum of four components, each corresponding to a given Zn species (30). To confirm this conclusion and to calculate the relative proportion of each sequestering mineral, the experimental EXAFS spectrum was least-squares fitted with linear combinations of reference EXAFS spectra from our database. For each simulation, all references were considered. The best one-component spectral agreement was obtained with Zn-containing phyllosilicate, suggesting that this species is most abundant (Figure 3). However, differences can be seen clearly by eye alone, justifying multiple-species fits. Zn-sorbed goethite was added in a two-component analysis, Zn-sorbed hexagonal birnessite was added in a three-component analysis, and finally Zn-containing lithiophorite (Figure 4) was added. The degree of improvement of the spectral match as given by the value of the residual decreases with the number of components, since minor species are added last and contribute less to the total experimental spectrum. In this series of simulations, the addition of second (phyllosilicate) and third (birnessite) components significantly improved the simulation, but the fourth (lithiophorite) is more questionable. Ten percent of lithiophorite in the four-component fit corresponds to the accepted sensitivity of metal speciation by this multicomponent spectral-fitting approach (20, 30–32). We note, however, that the existence of the lithiophorite species was confirmed by μXRF and μXRD .

Speciation of Ni. Ni speciation could not be quantified by EXAFS because of very low concentrations and high Mn, Fe background scattering at the Ni K-edge. However, based on our μXRF analysis of six different soil nodules, we came to the conclusion that Ni is sequestered by goethite and lithiophorite. The high Ni partitioning into the nodules results directly from selective sequestration by iron and manganese oxides, the principal minerals that cause nodule formation. This geochemical association identified in soils parallels that known in oceanic nodules (33) and is compelling evidence for the location of nickel in one and the same definite cation site of the phyllosilicate crystal structure. Recently, Manceau et al. (13) showed that nickel substitutes for Mn^{3+} in the manganese layer of lithiophorite in soil nodules from France; therefore, nickel is likely sequestered by the same mechanism in these micronodules sampled from soils across the United States and Europe.

The difference in speciation of Zn and Ni provides a clue to the observed higher partitioning of Ni in the soil nodules over the soil matrix (8, 9). As stated above, nodules commonly form in soils with restricted internal drainage by the solubilization of Fe(II) and Mn(II) under reducing conditions, followed by precipitation as iron(III) and manganese(III,IV) oxides under oxidizing conditions. Consequently, concretions have the same quantities of phyllosilicates and coarse grains (quartz, feldspar, titanium oxides, ...) as does the soil matrix, but they contain a higher quantity of finely divided iron and manganese oxides that cement soil material together and reduce its porosity. Since Zn-bound phyllosilicate is the

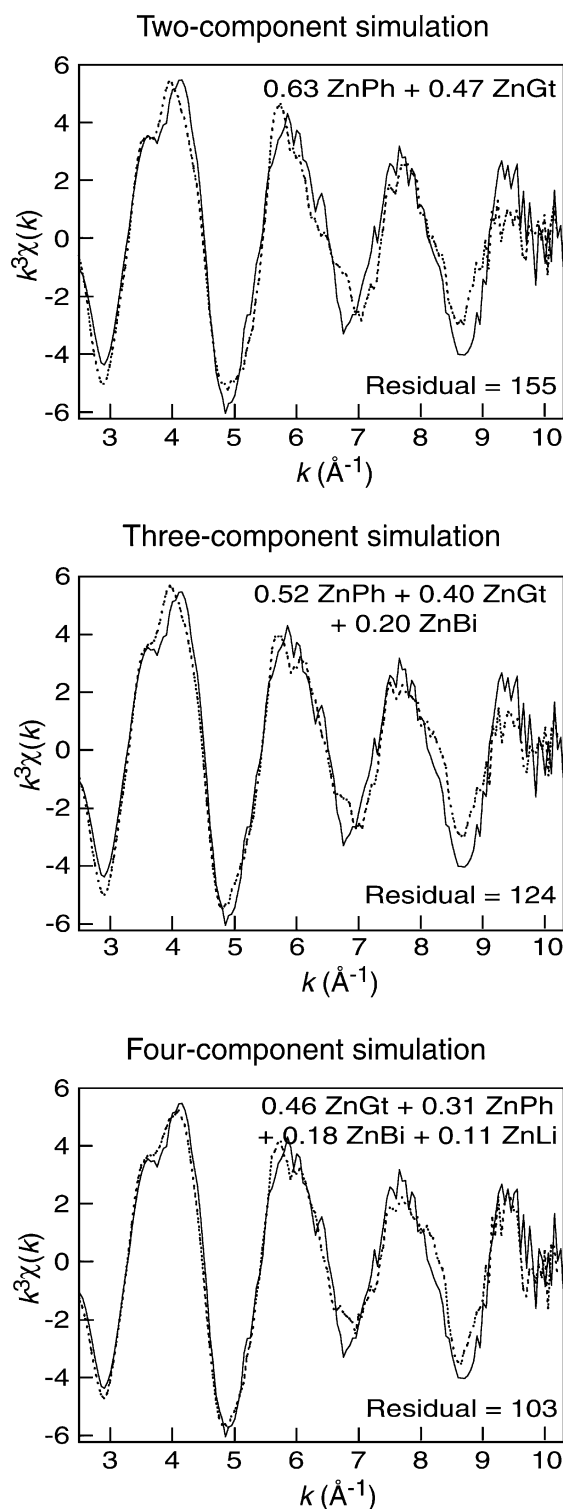


FIGURE 4. Multicomponent least-squares fitting of the nodule EXAFS spectrum (solid line) to a linear combination of reference spectra (dotted line). The best simulation was obtained for $45 \pm 10\%$ goethite + $30 \pm 10\%$ phyllosilicate + $20 \pm 10\%$ birnessite + $10 \pm 10\%$ lithiophorite. Simulations were optimized by minimizing the square difference between the data and the fit. Note that the addition of lithiophorite in the four-component fit decreased the percentage of phyllosilicate from $\sim 50\%$ to $\sim 30\%$ because these two references have similar EXAFS spectra since Zn is surrounded by "light" cations (Mg and Al) at similar distances (edge-sharing) in both structures (see Figure 3).

second most abundant species based on the four-component analysis and because this latter mineral is uniformly present

in the soil, Zn partitioning in nodules is necessarily limited. Conversely, the absence of phyllosilicate in ferromanganese coatings from river sediments may be the reason for high Zn partitioning into manganese oxides in these particles (10).

The results of this research may help to improve the efficiency of in situ technologies for remediating metal-contaminated soils. One such technology involves the addition of reactive materials that decrease metal availability, and one important question often posed by regulators is the durability of a treatment. The efficiency of each of the three groups of Zn species identified in this study, i.e., phyllosilicate, iron oxyhydroxide, and manganese oxide, has been evaluated, and in all cases separate application to contaminated soils led to a marked reduction of metal bioavailability and toxicity (34–36). Enhanced remediation should be obtained if these three families of minerals were applied altogether (37). Such a synergetic effect was observed recently for an As-contaminated gold mine spoil by the co-addition of steel shot (zerovalent Fe), beringite (phyllosilicate), and municipal compost (38). Beringite was used for its alkaline and sorptive properties and the compost to fertilize the spoil. Since manganese, more than iron, has a strong ability to segregate as a result of changing redox conditions during pedogenesis and forms various kinds of indurated precipitates (crusts, globules, nodules, ...), its co-addition to phyllosilicate and iron (either in elemental or oxide form) should increase the immobilization of metal contaminants and decrease their uptake by organisms.

Acknowledgments

The nodule samples were kindly provided by F. E. Rhoton and J. M. Bigham. The authors thank the ESRF and the ALS for beamtime and J. L. Hazemann and O. Proux for assistance during EXAFS measurements. A.M. is grateful to LBNL for financial support from the Laboratory Directed Research and Development Program. This work was partly supported by the Director, Office of Energy Research, Office of Basic Energy Sciences, Materials Sciences Division of the U.S. Department of Energy under Contract DE-AC03-76SF00098.

Literature Cited

- (1) McKenzie, R. M. In *Minerals in Soil Environments*; Dixon, J. B., Weed, S. B., Eds.; Soil Science Society of America: Madison, WI, 1989; pp 439–465.
- (2) White, G. N.; Dixon, J. B. *Soil Sci. Soc. Am. J.* **1996**, *60*, 1254–1262.
- (3) Post, J. E. *Proc. Natl. Acad. Sci. U.S.A.* **1999**, *96*, 3447–3454.
- (4) Lindbo, D. L.; Rhoton, F. E.; Hudnall, W. H.; Smeck, N. E.; Bigham, J. M.; Tyler, D. D. *Soil Sci. Soc. Am. J.* **2000**, *64*, 1713–1722.
- (5) Schwertmann, U.; Fanning, D. S. *Soil Sci. Soc. Am. J.* **1976**, *40*, 731–738.
- (6) Glasby, G. P.; Rankin, P. C.; Meylan, M. A. *Pac. Sci.* **1979**, *33*, 103–115.
- (7) Tebo, B. M.; He, L. M. In *Mineral–Water Interfacial Reactions: Kinetics and Mechanisms*; Sparks, D. L., Grundl, T. J., Eds.; American Chemical Society: Washington, DC, 1998; pp 393–414.
- (8) Palumbo, B.; Bellanca, A.; Neri, R.; Roe, M. J. *Chem. Geol.* **2001**, *173*, 257–269.
- (9) Childs, C. W. *Geoderma* **1975**, *13*, 141–152.
- (10) Hudson-Edwards, K. A. In *Environmental Mineralogy: Microbial Interactions, Anthropogenic Influences, Contaminated Land and Waste Management*; Cotter-Howells, J. D., Campbell, L. S., Valsami-Jones, E., Batchelder, M., Eds.; Mineralogical Society: London, 2000; Vol. 9.
- (11) Manceau, A.; Marcus, M. A.; Tamura, N. In *Applications of Synchrotron Radiation in Low-Temperature Geochemistry and Environmental Science*; Fenter, P., Sturchio, N. C., Eds.; Reviews in Mineralogy and Geochemistry; Mineralogical Society of America: Washington, DC, 2002; Vol. 49.
- (12) Rhoton, F. E.; Bigham, J. M.; Schulze, D. G. *Soil Sci. Soc. Am. J.* **1993**, *57*, 1386–1392.
- (13) Manceau, A.; Tamura, N.; Marcus, M. A.; MacDowell, A. A.; Celestre, R. S.; Sublett, R. E.; Sposito, G.; Padmore, H. A. *Am. Mineral.* **2002**, *87*, 1494–1499.
- (14) Schlegel, M. L.; Manceau, A.; Charlet, L.; Chateigner, D.; Hazemann, J. L. *Geochim. Cosmochim. Acta* **2001**, *65*, 4155–4170.
- (15) Schlegel, M. L.; Manceau, A.; Charlet, L.; Hazemann, J. L. *Am. J. Sci.* **2001**, *301*, 798–830.
- (16) Sarret, G.; Manceau, A.; Spadini, L.; Roux, J. C.; Hazemann, J. L.; Soldo, Y.; Eybert-Bérard, L.; Menthonnex, J. *J. Environ. Sci. Technol.* **1998**, *32*, 1648–1655.
- (17) Sarret, G.; Manceau, A.; Cuny, D.; Van Haluwyn, C.; Déruelle, S.; Hazemann, J. L.; Eybert-Bérard, L.; Menthonnex, J. *J. Environ. Sci. Technol.* **1998**, *32*, 3325–3330.
- (18) Sarret, G.; Vangronsveld, J.; Manceau, A.; Musso, M.; Hazemann, J. L.; Menthonnex, J. *J. Environ. Sci. Technol.* **2001**, *35*, 2854–2859.
- (19) Manceau, A.; Lanson, B.; Schlegel, M. L.; Hargé, J. C.; Musso, M.; Eybert-Bérard, L.; Hazemann, J. L.; Chateigner, D.; Lambelle, G. M. *Am. J. Sci.* **2000**, *300*, 289–343.
- (20) Isaure, M. P.; Laboudigue, A.; Manceau, A.; Sarret, G.; Tiffreau, C.; Trocellier, P.; Hazemann, J. L.; Chateigner, D. *Geochim. Cosmochim. Acta* **2002**, *66*, 1549–1567.
- (21) Manceau, A.; Lanson, B.; Drits, V. A. *Geochim. Cosmochim. Acta* **2002**, *66*, 2639–2663.
- (22) Manceau, A.; Schlegel, M. L.; Musso, M.; Sole, V. A.; Gauthier, C.; Petit, P. E.; Trolard, F. *Geochim. Cosmochim. Acta* **2000**, *64*, 3643–3661.
- (23) Varentsov, I. M. *Mar. Geol.* **1991**, *96*, 53–70.
- (24) Vodyanitskii, Y. N.; Lesovaya, S. N.; Sivtsov, A. V. *Eur. Soil Sci.* **2001**, *34*, 774–782.
- (25) Taylor, R. M. *J. Soil Sci.* **1968**, *19*, 77–80.
- (26) Chukhrov, F. V.; Gorshkov, A. I. *Trans. R. Soc., Edinburgh* **1981**, *72*, 195–200.
- (27) Uzochukwu, G. A.; Dixon, J. B. *Soil Sci. Soc. Am. J.* **1986**, *50*, 1358–1363.
- (28) Tokashiki, Y.; Dixon, J. B.; Golden, D. C. *Soil Sci. Soc. Am. J.* **1986**, *50*, 1079–1084.
- (29) Golden, D. C.; Dixon, J. B.; Kanehiro, Y. *Aust. J. Soil Res.* **1993**, *31*, 51–66.
- (30) Manceau, A.; Boisset, M. C.; Sarret, G.; Hazemann, J. L.; Mench, M.; Cambier, P.; Prost, R. *Environ. Sci. Technol.* **1996**, *30*, 1540–1552.
- (31) Ostergren, J. D.; Brown, G. E.; Parks, G. A.; Tingle, T. N. *Environ. Sci. Technol.* **1999**, *33*, 1627–1636.
- (32) Morin, G.; Juillot, F.; Ildefonse, P.; Calas, G.; Samama, J. C.; Chevallier, P.; Brown, G. E. *Am. Mineral.* **2001**, *86*, 92–104.
- (33) Usui, A. *Nature* **1979**, *279*, 411–413.
- (34) Mench, M.; Manceau, A.; Vangronsveld, J.; Clijsters, H.; Mocquot, B. *Agronomie* **2000**, *20*, 383–397.
- (35) Mench, M.; Vangronsveld, J.; Didier, V.; Clijsters, H. *Environ. Pollut.* **1994**, *86*, 279–286.
- (36) Vangronsveld, J.; Van Assche, F.; Clijsters, H. *Environ. Pollut.* **1995**, *87*, 51–59.
- (37) Hettiarachchi, G. M.; Pierzynski, G. M.; Ransom, M. D. *Environ. Sci. Technol.* **2000**, *34*, 4614–4619.
- (38) Mench, M.; Bussière, S.; Boisson, J.; Castaing, E.; Vangronsveld, J.; Rutters, A.; De Koe, T.; Bleeker, P.; Assunção, A.; Manceau, A. *Plant Soil* (in press).
- (39) Lanson, B.; Drits, V. A.; Gaillot, A. C.; Silvester, E.; Plancon, A.; Manceau, A. *Am. Mineral.* **2002**, *87*, 1631–1645.

Received for review April 25, 2002. Revised manuscript received October 14, 2002. Accepted October 21, 2002.

ES025748R